

Measurement of W-pair production in $e^{+}e^{-}$ collisions at centre-of-mass energies from 183 to 209 GeV

Journal Article**Author(s):**

ALEPH Collaboration; Schael, Stefan; Dissertori, Günther; et al.

Publication date:

2004-12

Permanent link:

<https://doi.org/10.3929/ethz-b-000034423>

Rights / license:

[Creative Commons Attribution 4.0 International](#)

Originally published in:

The European Physical Journal C 38(2), <https://doi.org/10.1140/epjc/s2004-02048-3>

Measurement of W -pair production in e^+e^- collisions at centre-of-mass energies from 183 to 209 GeV

The ALEPH Collaboration

S. Schael

Physikalisches Institut der RWTH-Aachen, 52056 Aachen, Germany

R. Barate, R. Brunelière, I. De Bonis, D. Decamp, C. Goy, S. Jézéquel, J.-P. Lees, F. Martin, E. Merle, M.-N. Minard, B. Pietrzyk, B. Trocmé

Laboratoire de Physique des Particules (LAPP), IN²P³-CNRS, 74019 Annecy-le-Vieux Cedex, France

S. Bravo, M.P. Casado, M. Chmeissani, J.M. Crespo, E. Fernandez, M. Fernandez-Bosman, Ll. Garrido¹⁵, M. Martinez, A. Pacheco, H. Ruiz

Institut de Física d'Altes Energies, Universitat Autònoma de Barcelona, 08193 Bellaterra (Barcelona), Spain⁷

A. Colaleo, D. Creanza, N. De Filippis, M. de Palma, G. Iaselli, G. Maggi, M. Maggi, S. Nuzzo, A. Ranieri, G. Raso²⁴, F. Ruggieri, G. Selvaggi, L. Silvestris, P. Tempesta, A. Tricomi³, G. Zito

Dipartimento di Fisica, INFN Sezione di Bari, 70126 Bari, Italy

X. Huang, J. Lin, Q. Ouyang, T. Wang, Y. Xie, R. Xu, S. Xue, J. Zhang, L. Zhang, W. Zhao

Institute of High Energy Physics, Academia Sinica, Beijing, The People's Republic of China⁸

D. Abbaneo, T. Barklow²⁶, O. Buchmüller²⁶, M. Cattaneo, B. Clerbaux²³, H. Drevermann, R.W. Forty, M. Frank, F. Gianotti, J.B. Hansen, J. Harvey, D.E. Hutchcroft³⁰, P. Janot, B. Jost, M. Kado², P. Mato, A. Moutoussi, F. Ranjard, L. Rolandi, D. Schlatter, G. Sguazzoni, F. Teubert, A. Valassi, I. Videau

European Laboratory for Particle Physics (CERN), 1211 Geneva 23, Switzerland

F. Badaud, S. Dessagne, A. Falvard²⁰, D. Fayolle, P. Gay, J. Jousset, B. Michel, S. Monteil, D. Pallin, J.M. Pascolo, P. Perret

Laboratoire de Physique Corpusculaire, Université Blaise Pascal, IN²P³-CNRS, Clermont-Ferrand, 63177 Aubière, France

J.D. Hansen, J.R. Hansen, P.H. Hansen, A.C. Kraan, B.S. Nilsson

Niels Bohr Institute, 2100 Copenhagen, DK-Denmark⁹

A. Kyriakis, C. Markou, E. Simopoulou, A. Vayaki, K. Zachariadou

Nuclear Research Center Demokritos (NRCD), 15310 Attiki, Greece

A. Blondel¹², J.-C. Brient, F. Machefert, A. Rougé, H. Videau

Laboratoire Leprince-Ringuet, Ecole Polytechnique, IN²P³-CNRS, 91128 Palaiseau Cedex, France

V. Ciulli, E. Focardi, G. Parrini

Dipartimento di Fisica, Università di Firenze, INFN Sezione di Firenze, 50125 Firenze, Italy

A. Antonelli, M. Antonelli, G. Bencivenni, F. Bossi, G. Capon, F. Cerutti, V. Chiarella, P. Laurelli, G. Mannocchi⁵, G.P. Murtas, L. Passalacqua

Laboratori Nazionali dell'INFN (LNF-INFN), 00044 Frascati, Italy

J. Kennedy, J.G. Lynch, P. Negus, V. O'Shea, A.S. Thompson

Department of Physics and Astronomy, University of Glasgow, Glasgow G12 8QQ, United Kingdom¹⁰

S. Wasserbaech

Utah Valley State College, Orem, UT 84058, USA

R. Cavanaugh⁴, S. Dhamotharan²¹, C. Geweniger, P. Hanke, V. Hepp, E.E. Kluge, A. Putzer, H. Stenzel, K. Tittel, M. Wunsch¹⁹

Kirchhoff-Institut für Physik, Universität Heidelberg, 69120 Heidelberg, Germany¹⁶

R. Beuselinck, W. Cameron, G. Davies, P.J. Dornan, M. Girone¹, N. Marinelli, J. Nowell, S.A. Rutherford, J.K. Sedgbeer, J.C. Thompson¹⁴, R. White
Department of Physics, Imperial College, London SW7 2BZ, United Kingdom¹⁰

V.M. Ghete, P. Girtler, E. Kneringer, D. Kuhn, G. Rudolph
Institut für Experimentalphysik, Universität Innsbruck, 6020 Innsbruck, Austria¹⁸

E. Bouhova-Thacker, C.K. Bowdery, D.P. Clarke, G. Ellis, A.J. Finch, F. Foster, G. Hughes, R.W.L. Jones, M.R. Pearson, N.A. Robertson, M. Smizanska
Department of Physics, University of Lancaster, Lancaster LA1 4YB, United Kingdom¹⁰

O. van der Aa, C. Delaere²⁸, G. Leibenguth³¹, V. Lemaitre²⁹
Institut de Physique Nucléaire, Département de Physique, Université Catholique de Louvain, 1348 Louvain-la-Neuve, Belgium

U. Blumenschein, F. Hölldorfer, K. Jakobs, F. Kayser, K. Kleinknecht, A.-S. Müller, B. Renk, H.-G. Sander, S. Schmeling, H. Wachsmuth, C. Zeitnitz, T. Ziegler
Institut für Physik, Universität Mainz, 55099 Mainz, Germany¹⁶

A. Bonissent, P. Coyle, C. Curtil, A. Ealet, D. Fouchez, P. Payre, A. Tilquin
Centre de Physique des Particules de Marseille, Univ Méditerranée, IN²P³-CNRS, 13288 Marseille, France

F. Ragusa
Dipartimento di Fisica, Università di Milano e INFN Sezione di Milano, 20133 Milano, Italy.

A. David, H. Dietl³², G. Ganis²⁷, K. Hüttmann, G. Lütjens, W. Männer³², H.-G. Moser, R. Settles, M. Villegas, G. Wolf
Max-Planck-Institut für Physik, Werner-Heisenberg-Institut, 80805 München, Germany^p

J. Boucrot, O. Callot, M. Davier, L. Duflot, J.-F. Grivaz, Ph. Heusse, A. Jacholkowska⁶, L. Serin, J.-J. Veillet
Laboratoire de l'Accélérateur Linéaire, Université de Paris-Sud, IN²P³-CNRS, 91898 Orsay Cedex, France

P. Azzurri, G. Bagliesi, T. Boccali, L. Foà, A. Giammanco, A. Giassi, F. Ligabue, A. Messineo, F. Palla, G. Sanguinetti, A. Sciabà, P. Spagnolo, R. Tenchini, A. Venturi, P.G. Verдини
Dipartimento di Fisica dell'Università, INFN Sezione di Pisa, e Scuola Normale Superiore, 56010 Pisa, Italy

O. Awunor, G.A. Blair, G. Cowan, A. Garcia-Bellido, M.G. Green, T. Medcalf, A. Misiejuk, J.A. Strong, P. Teixeira-Dias
Department of Physics, Royal Holloway & Bedford New College, University of London, Egham, Surrey TW20 OEX, United Kingdom¹⁰

R.W. Clift, T.R. Edgecock, P.R. Norton, I.R. Tomalin, J.J. Ward
Particle Physics Dept., Rutherford Appleton Laboratory, Chilton, Didcot, Oxon OX11 0QX, United Kingdom¹⁰

B. Bloch-Devaux, D. Boumediene, P. Colas, B. Fabbro, E. Lançon, M.-C. Lemaire, E. Locci, P. Perez, J. Rander, B. Tuchming, B. Vallage
CEA, DAPNIA/Service de Physique des Particules, CE-Saclay, 91191 Gif-sur-Yvette Cedex, France¹⁷

A.M. Litke, G. Taylor
Institute for Particle Physics, University of California at Santa Cruz, Santa Cruz, CA 95064, USA²²

C.N. Booth, S. Cartwright, F. Combley²⁵, P.N. Hodgson, M. Lehto, L.F. Thompson
Department of Physics, University of Sheffield, Sheffield S3 7RH, United Kingdom¹⁰

A. Böhrer, S. Brandt, C. Grupen, J. Hess, A. Ngac, G. Prange
Fachbereich Physik, Universität Siegen, 57068 Siegen, Germany¹⁶

C. Borean, G. Giannini
Dipartimento di Fisica, Università di Trieste e INFN Sezione di Trieste, 34127 Trieste, Italy

H. He, J. Putz, J. Rothberg
Experimental Elementary Particle Physics, University of Washington, Seattle, WA 98195 USA

S.R. Armstrong, K. Berkelman, K. Cranmer, D.P.S. Ferguson, Y. Gao¹³, S. González, O.J. Hayes, H. Hu, S. Jin, J. Kile, P.A. McNamara III, J. Nielsen, Y.B. Pan, J.H. von Wimmersperg-Toeller, W. Wiedenmann, J. Wu, Sau Lan Wu, X. Wu, G. Zobernig
Department of Physics, University of Wisconsin, Madison, WI 53706, USA¹¹

G. Dissertori
Institute for Particle Physics, ETH Hônggerberg, 8093 Zürich, Switzerland

Received: 1 October 2004 /

Published online: 15 November 2004 – © Springer-Verlag / Società Italiana di Fisica 2004

Abstract. The W^+W^- production cross section is measured from a data sample corresponding to a total integrated luminosity of 683 pb^{-1} , collected by the ALEPH experiment at LEP at centre-of-mass energies from 183 to 209 GeV. Individual cross sections for the different topologies arising from W decays into leptons or hadrons, as well as the total W-pair cross section are given at eight centre-of-mass energies. The results are found to be in agreement with recently developed Standard Model calculations at the one percent level. The hadronic branching fraction of the W boson is measured to be $B(W \rightarrow q\bar{q}) = 67.13 \pm 0.37\text{ (stat.)} \pm 0.15\text{ (syst.)}\%$, from which the CKM matrix element $|V_{cs}|$ is determined to be $0.958 \pm 0.017\text{ (stat.)} \pm 0.008\text{ (syst.)}$.

¹ Also at CERN, 1211 Geneva 23, Switzerland.

² Now at Fermilab, PO Box 500, MS 352, Batavia, IL 60510, USA

³ Also at Dipartimento di Fisica di Catania and INFN Sezione di Catania, 95129 Catania, Italy.

⁴ Now at University of Florida, Department of Physics, Gainesville, Florida 32611-8440, USA

⁵ Also IFSI sezione di Torino, CNR, Italy.

⁶ Also at Groupe d'Astroparticules de Montpellier, Université de Montpellier II, 34095, Montpellier, France.

⁷ Supported by CICYT, Spain.

⁸ Supported by the National Science Foundation of China.

⁹ Supported by the Danish Natural Science Research Council.

¹⁰ Supported by the UK Particle Physics and Astronomy Research Council.

¹¹ Supported by the US Department of Energy, grant DE-FG0295-ER40896.

¹² Now at Departement de Physique Corpusculaire, Université de Genève, 1211 Genève 4, Switzerland.

¹³ Also at Department of Physics, Tsinghua University, Beijing, The People's Republic of China.

¹⁴ Supported by the Leverhulme Trust.

¹⁵ Permanent address: Universitat de Barcelona, 08208 Barcelona, Spain.

¹⁶ Supported by Bundesministerium für Bildung und Forschung, Germany.

¹⁷ Supported by the Direction des Sciences de la Matière, C.E.A.

¹⁸ Supported by the Austrian Ministry for Science and Transport.

¹⁹ Now at SAP AG, 69185 Walldorf, Germany

²⁰ Now at Groupe d'Astroparticules de Montpellier, Université de Montpellier II, 34095 Montpellier, France.

²¹ Now at BNP Paribas, 60325 Frankfurt am Mainz, Germany

²² Supported by the US Department of Energy, grant DE-FG03-92ER40689.

²³ Now at Institut Inter-universitaire des hautes Energies (IHE), CP 230, Université Libre de Bruxelles, 1050 Bruxelles, Belgique

²⁴ Now at Dipartimento di Fisica e Tecnologia Relative, Università di Palermo, Palermo, Italy.

²⁵ Deceased.

²⁶ Now at SLAC, Stanford, CA 94309, U.S.A

²⁷ Now at CERN, 1211 Geneva 23, Switzerland

²⁸ Research Fellow of the Belgium FNRS

²⁹ Research Associate of the Belgium FNRS

³⁰ Now at Liverpool University, Liverpool L69 7ZE, United Kingdom

1 Introduction

This paper describes the measurement of the W-pair production cross section in e^+e^- collisions with the ALEPH detector at LEP, for centre-of-mass (CM) energies from 183 to 209 GeV. A consistent analysis was performed with all data taken in the years 1997 to 2000. The present result therefore supersedes the previously published results [1] which were based on the data collected in 1997 and 1998. The WW events are identified in all possible final states arising from W decays into leptons and hadrons: fully leptonic ($\ell\nu\ell\nu$), semileptonic ($\ell\nu q\bar{q}$) and fully hadronic ($4q$). This enables the W branching fractions and, indirectly, the Wcs coupling to be determined.

The results presented here are expressed in terms of the so-called $CC03$ cross section [2]. Theoretically, the $CC03$ cross section is computed from the set of three Feynman diagrams leading to four-fermion final states through two resonating W's, with either ν_e exchange in the t channel or Z/γ exchange in the s channel. In practice, the W^+W^- candidate events, selected as four-fermion final states in the data, arise from (i) the gauge-invariant set of all four-fermion production graphs yielding final states compatible with W^+W^- production and their interference (the corresponding events are called $4f$ events in the following); and (ii) some background from four-fermion production graphs yielding final states not compatible with W^+W^- production and some non-four-fermion background.

As a consequence, the measured cross section has to be corrected for the expected background, for the difference between the predicted $4f$ and $CC03$ cross sections in the selection acceptance (labelled $4f-CC03$ in the following) and for the $CC03$ selection efficiency. The result is the measured WW (or $CC03$) cross section.

An experimental precision at the percent level requires a careful evaluation of higher order corrections. Several approaches were discussed in a workshop held at CERN in 1999–2000 [3]. Their predictions agree within the estimated theoretical uncertainty of about 0.5%.

The ALEPH data sample at LEP2 corresponds to a total integrated luminosity of $682.6 \pm 0.4\text{ (stat.)} \pm 2.0\text{ (syst.) pb}^{-1}$. The results presented here are given

³¹ Supported by the Federal Office for Scientific, Technical and Cultural Affairs through the Interuniversity Attraction Pole P5/27

³² Now at Henryk Niewodniczski Institute of Nuclear Physics, Polish Academy of Sciences, Cracow, Poland

Table 1. Overview of the CM energies and corresponding data integrated luminosity

Year	Energy (GeV)	Luminosity and its total error (pb^{-1})
1997	182.65	56.8 ± 0.3
1998	188.63	174.2 ± 0.8
1999	191.58	28.9 ± 0.1
	195.52	79.9 ± 0.4
	199.52	86.3 ± 0.4
	201.62	41.9 ± 0.2
2000	204.86	81.4 ± 0.4
	206.53	133.2 ± 0.6

for eight different CM energies. For the last year of data taking, as the CM energy was continuously increased, the dataset was split into two subsamples, the first integrating data at energies from 202.5 GeV to 205.5 GeV, and the second including all data taken at energies above 205.5 GeV. The breakdown is given in Table 1.

2 The ALEPH detector

A detailed description of the ALEPH detector can be found in [4] and of its performance in [5]. Charged particles are detected in the central part, which consists of a precision silicon vertex detector (VDET), a cylindrical drift chamber (ITC) and a large time projection chamber (TPC), measuring altogether up to 31 space points along the charged particle trajectories. A 1.5 T axial magnetic field is provided by a superconducting solenoidal coil. Charged particle transverse momenta are reconstructed with a $1/p_T$ resolution of $(6 \times 10^{-4} \oplus 5 \times 10^{-3}/p_T)$ (GeV/c) $^{-1}$. The charged particle tracks used in the present analysis (and simply called *tracks*) are reconstructed with at least four hits in the TPC, and originate from within a cylinder of length 20 cm and radius 2 cm coaxial with the beam and centred at the nominal collision point.

In addition to its rôle as a tracking device, the TPC also measures the specific energy loss by ionization dE/dx . It allows low momentum electrons to be separated from other charged particle species by more than three standard deviations.

Electrons (and photons) are also identified by the characteristic longitudinal and transverse developments of the associated showers in the electromagnetic calorimeter, a 22 radiation length thick sandwich of lead planes and proportional wire chambers with fine read-out segmentation. A relative energy resolution of $0.18/\sqrt{E}$ (E in GeV) is achieved for isolated electrons and photons.

Muons are identified by their characteristic penetration pattern in the hadron calorimeter, a 1.2 m thick yoke interleaved with 23 layers of streamer tubes, together with two surrounding double-layers of muon chambers. In association with the electromagnetic calorimeter, the hadron calorimeter also provides a measurement of the hadronic energy with a relative resolution of $0.85/\sqrt{E}$ (E in GeV).

The total visible energy is measured with an energy-flow reconstruction algorithm which combines all the above measurements [5]. The relative resolution on the total visible energy is $0.60/\sqrt{E}$ for high multiplicity final states. In addition to the total visible-energy measurement, the energy-flow reconstruction algorithm also provides a list of reconstructed objects, classified as charged particles, photons and neutral hadrons, and called *energy-flow objects* in the following. Unless otherwise specified, these energy-flow objects are the basic entities used in the present analysis.

Below polar angles of 12° and down to 34 mrad from the beam axis, the acceptance is closed at both ends of the experiment by the luminosity calorimeter (LCAL) [6] and a tungsten-silicon calorimeter (SICAL) [7] originally designed for the LEP 1 luminosity measurement. The dead regions between the two LCAL modules at each end are covered by pairs of scintillators. The luminosity is measured with small-angle Bhabha events with the LCAL with an uncertainty smaller than 0.5%. The Bhabha cross section [8] in the LCAL acceptance varies from 4.6 nb at 183 GeV to 3.6 nb at 207 GeV.

3 Monte Carlo simulation

3.1 Monte Carlo generators

Four-fermion events compatible with WW final states ($4f$ events) were generated using KoralW 1.51 [9]. These events therefore include all single W ($W e \nu$) final states and some ZZ and Zee final states. The $q\bar{q}$ final states were fragmented into parton showers and hadronized using JETSET 7.4 [10] or PYTHIA 6.1 [11].

Background events were simulated by a variety of event generators.

- Bhabha events were produced using the program BHWIDE 1.01 [12].
- Dimuon, $\mu^+\mu^-$, and ditau, $\tau^+\tau^-$, events were generated using KK 4.14 [13]. Initial and final state radiative corrections and their interference are included. This generator was also used for $q\bar{q}$ pairs with initial state radiation. The final state radiation was however handled by PYTHIA in the parton shower step and interference was therefore not included.
- The remaining ZZ and Zee events, such as $u\bar{u}u\bar{u}$, $\mu^+\mu^-e^+e^-$, etc., not compatible with WW final states were generated with PYTHIA 6.1.
- Two-photon interaction processes ($e^+e^- \rightarrow e^+e^- X$), referred to as $\gamma\gamma$ events, were generated with the PHOT02 generator [14]. When X is a pair of leptons, a QED calculation was used with preselection cuts to enrich the WW-like selected region. When X is a multi-hadronic state, a dedicated setup of PYTHIA was used to generate untagged events where the initial electrons are scattered within 12° of the beam. The complementary tagged events where at least one of the scattered electrons can be identified in the detector were generated with HERWIG 6.2 [15].

The studies of fragmentation and final state interactions (FSI) such as Bose-Einstein correlations or colour reconnection require dedicated event samples to be generated. Whenever technically possible, a global tuning of fragmentation parameters was performed using data collected at the Z. To reduce the sensitivity to statistical fluctuations, a special procedure was followed in the comparison of different fragmentation models. The event generation was stopped at the parton level and the same event was subjected to fragmentation according to JETSET 7.4, HERWIG 6.2 or ARIADNE 4.10 [16]. A similar procedure was applied for the FSI investigations, with the same parton-level events reprocessed using alternatively:

- the JETSET models SKI, SKII and SKII', for colour reconnection between W's [17];
- a model for hadronic string reinteractions within and between W's based on a generalised area law (GAL) [18] using PYTHIA;
- the HERWIG model with FSI within and between W's with 11% colour reconnection probability;
- the ARIADNE models with colour reconnections within and between W's;
- PYTHIA for the Bose-Einstein correlations within and between W's using the model BE32 [19].

In total, more than 200 million events were generated for all mentioned processes at eight CM energies and processed through the complete chain of detector simulation and event reconstruction. The detector simulation took into account variations in the response of the apparatus from year to year.

3.2 Event reweighting

The $4f$ events generated by KORALW are unweighted events. The n_{4f} events accepted by the WW event selection correspond to a cross section σ_{4f} . To determine the $4f$ - $CC03$ difference and the $CC03$ event selection efficiency, a reweighting technique is used.

Each selected $4f$ event is reweighted by the ratio w_i of the matrix element squared computed with the sole set of $CC03$ diagrams to that computed with the whole set of $4f$ diagrams, to give a sample of (weighted) $CC03$ events. The $4f$ - $CC03$ difference is obtained by

$$4f-CC03 = \sigma_{4f} \sum_{i=1}^{n_{4f}} (1 - w_i).$$

The $CC03$ events are further reweighted by the $\mathcal{O}(\alpha)$ correction using the Double Pole Approximation (DPA) from YFSWW3 [20]. Such a correction is not applied to the non- $CC03$ diagrams. The ratio of the event weight sums after and before the WW event selection is the $CC03$ selection efficiency.

4 Selection of W-pair candidates

The event selection in each topology follows closely the analysis described in [1], apart from the $WW \rightarrow \tau\nu q\bar{q}$ se-

lection for which a new analysis with an upgraded tau reconstruction has been designed. Whenever justified, selection criteria are reoptimized at each energy. Fully leptonic, semileptonic and fully hadronic event selections developed below are mutually exclusive. Unless otherwise specified, the uncertainties quoted in this section are statistical only.

4.1 Electron and muon identification

Electrons and muons are identified using the standard algorithms [5]. For electrons, the complementary measurements of dE/dx from the TPC and the longitudinal and transverse shape of the shower of the energy deposition measured in ECAL are used to build the normally distributed estimators R_I , R_L and R_T . These estimators are calibrated as a function of the electron momentum and polar angle for data and simulation using Bhabha events from LEP1 and LEP2, with electron energies from 20 to 100 GeV. To identify a track as an electron, the estimators R_I and R_L are required to be greater than -2.5 , while R_T must be greater than -8 . In ECAL crack regions, these criteria are supplemented by the requirement that the number of fired HCAL planes does not exceed ten.

The measured momentum of the electrons is improved by combining it with the energy deposits in ECAL associated with both the electron and possible bremsstrahlung as it passes through the detector.

Muons are identified using the tracking capability of HCAL and the muon chambers. A road is defined by extrapolating tracks through the calorimeter and muon chambers and counting the number of observed hits on the digital readout strips. To reduce spurious signals from noise, a hit is considered only when fewer than four adjacent strips fire. For a track to be identified as a muon the total number of hits must exceed 40% of the number expected, with hits in at least five of the last ten planes and one of the last three. To eliminate misidentified muons due to hadron showers, cuts are made on the mean cluster multiplicity observed in the last half of the HCAL planes. Within the HCAL and muon chamber crack regions, muons are identified by requiring that the energy deposits in ECAL and HCAL be less than 10% of the track momentum and not greater than 1 and 5 GeV, respectively.

The identification efficiencies are measured using a double-tag method on lepton pairs, and yield efficiencies around 97% and 99% for electron and muon identification, respectively. The differences between data and simulation are applied as correction factors to the selection efficiencies. They take into account the polar angle distribution of electrons and muons from W decays. The corresponding numbers are given in Table 2.

4.2 $WW \rightarrow \ell\nu\ell\nu$ events

Fully leptonic events are characterized by two high energy acoplanar leptons (e , μ or τ) and substantial missing energy. The dominant background arises from $\gamma\gamma \rightarrow \ell\bar{\ell}$ and other non-WW-like four-fermion events, mainly $ZZ \rightarrow \ell\bar{\ell}\nu\bar{\nu}$.

Table 2. Data-simulation differences for lepton identification efficiencies used as correction factors in fully leptonic and semileptonic selections

Energy (GeV)	$\Delta\epsilon(e)$ (%)	$\Delta\epsilon(\mu)$ (%)
183	-0.56 ± 0.33	-0.14 ± 0.18
189	-0.43 ± 0.20	-0.17 ± 0.11
192–196	-0.70 ± 0.20	-0.10 ± 0.10
200–202	-0.69 ± 0.19	-0.09 ± 0.10
205–207	-0.39 ± 0.17	$+0.06 \pm 0.09$

Two selections for the $WW \rightarrow \ell\nu\ell\nu$ signal are used. They have similar overall efficiencies and background levels but differ in their sensitivities to individual lepton channels. In these selections, tracks are considered if their polar angle satisfies $|\cos\theta| < 0.95$.

The first selection does not make use of the lepton identification criteria. It is based on topological information and has similar sensitivity for all channels. Events are accepted if they contain two or four tracks with zero total electric charge. The four-track case is reduced to a two-jet topology by merging the three tracks with the smallest invariant mass. This triplet is interpreted as coming from a three-prong tau decay, and its mass is required to be smaller than $1.5 \text{ GeV}/c^2$. A photon veto is applied against radiative returns to the Z resonance with $Z \rightarrow \ell^+\ell^-$ by rejecting events with an isolated neutral energy flow ob-

ject remote from either lepton candidate. Doubly radiative returns to the Z resonance, with $Z \rightarrow \nu\bar{\nu}$ and a γ converted in the detector, are rejected by requiring that the angle between the two tracks be larger than 2° .

The second selection requires from two to six tracks which are then clustered using the JADE [21] algorithm with $y_{\text{cut}} = 0.0002$. Events with two or three jets are kept. The electron and muon identification criteria are then applied to classify the event into one of the six dilepton channels. A jet or a track is classified as “tau” if no electron/muon identification criteria is satisfied or if the identified lepton has an energy lower than 25 GeV. The energy of the most energetic jet must be within 20 - 80% of the beam energy. Three-jet events are rejected when the least energetic jet contains charged particles or has an energy larger than 5 GeV.

To remove $\gamma\gamma$ background events, cuts are made on the missing transverse momentum, the acoplanarity and the energy deposits close to the beam. For the last cut, events are rejected if there is any energy detected in SICAL, LCAL, ECAL, or HCAL within 14° of the beam axis or in the LCAL veto scintillators. This yields an inefficiency due to beam-related background and detector noise, not described in the simulation. It is measured to be in the range (1.7%–4.0%) using random trigger events recorded under the same conditions as physics events and applied as a correction to the selection efficiency.

Events are accepted as WW candidates if they pass either of the two selections. The combined average efficien-

Table 3. Summary of luminosity-weighted averaged results of the different event selections on Monte Carlo and data events. Efficiencies are given in percent for $CC03$ processes. In the qq qq column only events with a NN output greater than 0.3 are considered; the backgrounds listed include non-qq qq WW decays

Event selection and classification											
	ee	$e\mu$	$e\tau$	$\mu\mu$	$\mu\tau$	$\tau\tau$	eqq	μ qq	τ qq	qqqq	All
$e\nu e\nu$	57.7	0	9.2	0	0	0.8	–	–	–	–	67.7
$e\nu\mu\nu$	0	62.5	3.4	0	4.9	0.7	–	–	–	–	71.5
$e\nu\tau\nu$	5.0	4.1	49.9	0	0.3	4.2	–	–	–	–	63.5
Eff. for $\mu\nu\mu\nu$	0	0	0	64.7	7.2	0.6	–	–	–	–	72.5
WW $\rightarrow \mu\nu\tau\nu$	0	5.4	0.3	4.1	53.6	3.2	–	–	–	–	66.6
(%) $\tau\nu\tau\nu$	0.5	0.7	7.9	0.3	6.7	36.7	–	–	–	–	52.8
$e\nu$ qq	–	–	–	–	–	–	81.7	0.0	7.5	–	89.2
$\mu\nu$ qq	–	–	–	–	–	–	0.1	89.3	3.3	–	92.7
$\tau\nu$ qq	–	–	–	–	–	–	4.7	6.2	64.8	–	75.7
qqqq	–	–	–	–	–	–	–	–	–	90.0	90.0
Contribution (fb)											
$q\bar{q}$	0.	0.	0.	0.	0.	0.	57.2	12.7	123.3	1250.5	1443.7
ZZ	6.0	0.	3.5	6.6	3.4	5.0	8.3	19.9	63.0	196.3	312.0
$\gamma\gamma$	0.5	2.6	12.2	0.4	2.9	8.5	17.3	0.1	2.1	0.	46.6
Others	5.9	0.8	8.5	2.0	3.7	6.1	20.2	0.7	35.9	6.2	90.0
Total background	12.4	3.4	24.2	8.9	10.0	19.6	103.0	33.4	224.3	1453.1	1892.3
($4f$ – $CC03$)	11.4	7.9	12.6	3.6	3.7	4.8	58.9	3.0	88.6	177.3	371.8
Number of events											
observed events	98	191	189	99	184	91	1566	1643	1515	5696	11272
expected background	16.3	7.7	25.1	8.6	9.4	16.7	110.5	24.8	213.6	1112.9	1545.3

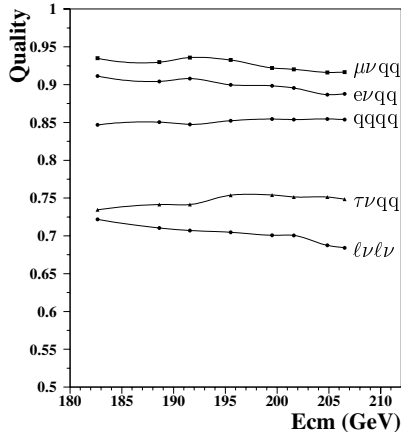


Fig. 1. Quality of the $CC03$ selection, defined as $\sqrt{\text{efficiency} \times \text{purity}}$, for all topologies as functions of CM energy. The statistical precision of the cross section measurement is optimal when the selection quality is maximized

cies and backgrounds are given in Table 3 together with the numbers of observed events.

The $CC03$ efficiency in the inclusive $\ell\nu\ell\nu$ channels is on average $66.2 \pm 0.15\%$. The energy dependence of the selection performance is shown in Fig. 1.

4.3 $WW \rightarrow \ell\nu qq$ events

The typical final state of a semileptonic WW event consists of an energetic lepton, large missing momentum and two energetic jets. The dominant background comes from $q\bar{q}(\gamma)$ events and other non- WW -like four-fermion events, mainly $ZZ \rightarrow \ell\ell qq$ and $Z\gamma$ final states. For the $\tau\nu qq$ channel, two-photon background must also be taken into account.

A preselection common to the three lepton topologies requires at least seven tracks in the event. Background from $q\bar{q}$ events is reduced by requiring the estimated missing energy to be greater than 35 GeV. The $Z\gamma$ events in which the photon is undetected are rejected by a cut on the missing longitudinal momentum.

4.3.1 $WW \rightarrow (e, \mu)\nu qq$ events

In addition to the common preselection, a tighter cut is used on the total visible energy and visible longitudinal momentum to further reject $Z\gamma$ events. The lepton candidate is chosen as the track with the largest $p^2(1 - \cos\theta_J)$ where p is the track momentum and θ_J is the angle from the track to the closest jet clustered from the remaining tracks using the Durham-P [22] algorithm ($y_{\text{cut}} = 0.0003$). Events are further considered if this lepton candidate satisfies either the electron or muon criteria defined in Sect. 4.1 and if the sum of the lepton and missing energy is greater than 30 GeV.

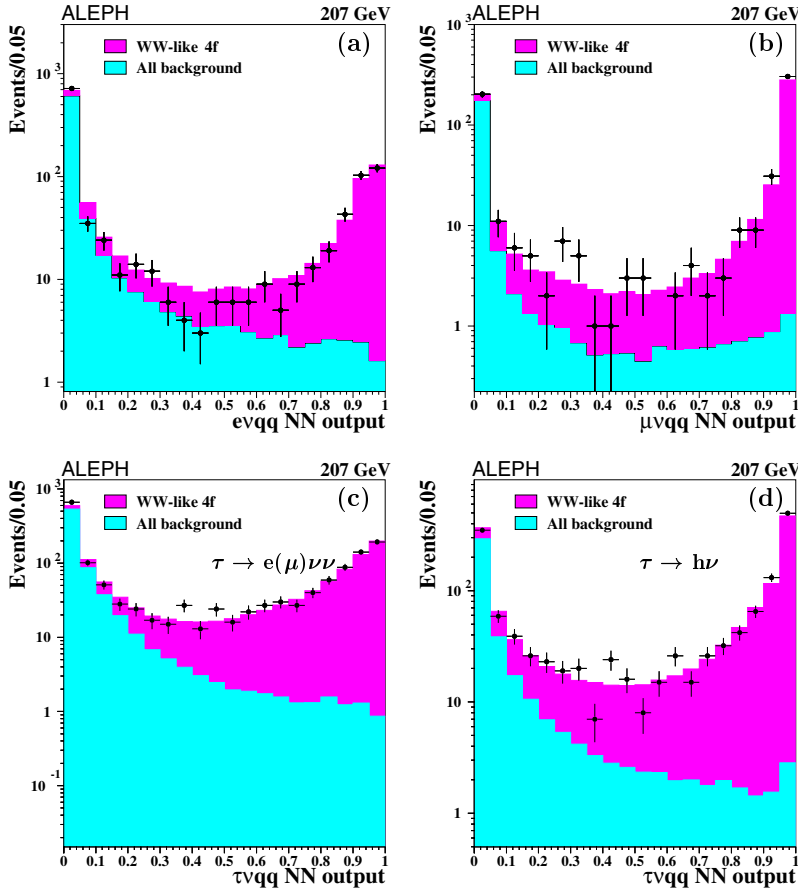


Fig. 2. Comparison of the NN output distributions at 207 GeV for data and simulation in the semileptonic channels after the preselection. The dots correspond to the data and the histograms to the predictions. Plots **a** and **b** correspond to the NN output distribution for $e\nu qq$ and $\mu\nu qq$ exclusive selections; plots **c** and **d** show the output distributions for the two $\tau\nu qq$ alternate selections before excluding the events selected by the $e(\mu)qq$ neural networks

Two different neural networks (NN) have been trained to select and classify $e\nu qq$ and $\mu\nu qq$ signal events. Both use three discriminant variables, the event transverse momentum, the lepton energy and the lepton isolation. The last variable is defined as $\log(\tan \theta_C/2) + \log(\tan \theta_F/2)$ where θ_C and θ_F are, respectively, the angle of the lepton to the closest track, and the opening angle of the largest cone centred on the lepton direction with less than 5 GeV of total energy.

The event is classified as $e\nu qq$ or $\mu\nu qq$ if the corresponding NN output value is larger than 0.60. Figures 2a and b show the NN output distributions for data and simulation at 207 GeV. The CM energy dependence of the selection performance is shown in Fig. 1.

4.3.2 $\tau\nu qq$ classification

A new selection has been designed, based on an improved reconstruction [23] of the tau. This yields a higher performance than in [1].

Leptonic τ decays are searched for by examining those events with e or μ candidates which fail the $e\nu qq$ or $\mu\nu qq$ NN cuts. These events are subjected to a similar three variable neural network but trained on leptonic tau decays. Events with the NN output greater than 0.6 are kept. The distribution of this NN output is shown in Fig. 2c together with the predictions from the simulation.

After removing the events which have satisfied any of the three variable NN selections for $e\nu qq$, $\mu\nu qq$ or $\tau\nu qq$ the remaining events are further examined for additional $\tau\nu qq$ final states. Use is made of the fact that one-prong tau decays are characterized by a low visible mass with mean about $0.75 \text{ GeV}/c^2$. The first step is to perform a jet clustering using the JADE [21] algorithm with a low $y_{\text{cut}} = (0.75/E_{\text{vis}})^2$. The tau candidate is defined as the jet which maximizes $p(1 - \cos \theta_j)$, where θ_j is the smallest angle with respect to other jets and p is the jet momentum. The event is then subjected to additional cuts, in particular the invariant mass of the hadronic recoil system to the tau candidate be in the range 60 to $105 \text{ GeV}/c^2$. For those events which fail, the procedure is repeated with increasingly higher values of y_{cut} in an attempt to find a suitable candidate. With this method, the simulation shows that in 75% of all $\tau\nu qq$ events the tau candidate jet contains only the tau charged decay products and in another 12% the tau is partly reconstructed.

If a tau-jet candidate is found, the event is subjected to further cuts to remove the main backgrounds. Most of the $\gamma\gamma$ interactions are rejected by requiring the visible mass of the event to be larger than $50 \text{ GeV}/c^2$ and the missing transverse momentum greater than $10 \text{ GeV}/c$. The event is divided into two hemispheres with respect to a plane perpendicular to the thrust axis. The acollinearity angle between the two hemispheres is required to be less than 175° to reject most of the $q\bar{q}$ background. About 80% of the events with a tau candidate satisfy these cuts but significant background remains, mainly from $q\bar{q}$ events. These events are then subjected to a 15 variable neural network; the variables are described in Appendix A. The NN output

is shown in Fig. 2d together with the expectations from simulation. The event is selected if the result is greater than 0.4.

4.3.3 Results of the selections

A total of 4724 candidate $\ell\nu qq$ events is selected in the data. Table 3 gives the average efficiencies, together with the expected background and the numbers of events selected. The luminosity-weighted average *CC03* efficiencies are $(89.2 \pm 0.10)\%$ for the $e\nu qq$ channel, $(92.7 \pm 0.10)\%$ for the $\mu\nu qq$ channel and $(75.7 \pm 0.13)\%$ for the $\tau\nu qq$ channel, with a total background of 361 fb. The CM energy dependence of the selection performance is shown in Fig. 1.

4.4 $WW \rightarrow qqqq$ events

A fully hadronic WW event shows a typical four-jet topology. For this topology there is also a large contribution from $q\bar{q}$ events with hard gluon radiation and other non WW-like four-fermion events. Only events not already selected are considered.

A first preselection step aims at removing events with a large undetected initial state (ISR) photon from radiative returns to the Z resonance by requiring that the absolute value of the total longitudinal momentum of all objects be less than $1.5(M_{\text{vis}} - M_Z)$ where M_{vis} is the observed visible mass. The particles are then forced to form four jets using the DURHAM-PE algorithm [22]. Only events where y_{34} , the transition from three to four jets, is larger than 0.001 are kept. To reject $q\bar{q}$ events with a visible ISR photon, none of the four jets can have more than 95% of electromagnetic energy in a one-degree cone around any particle included in the jet. Four-fermion final states in which one of the fermions is a charged lepton are rejected by requiring that the leading charged particle of each jet carries less than 90% of the jet energy.

The measured jet energies are corrected as a function of polar angle using factors determined from the data taken each year at the Z. The jet energies and directions are subsequently recomputed using a kinematic fit [24] which imposes energy and momentum conservation in the event.

A neural network [1] based on 14 variables, described in Appendix B, is trained at a number of CM energies. Figure 3 shows the NN output distribution for the data compared with the signal and backgrounds predicted by the simulation at two energies.

Table 3 summarizes the numbers of selected events, the average efficiencies and the predicted background cross section for the fully hadronic final state using an illustrative cut of 0.3 on the NN output. The CM energy dependence of the selection performance is shown in Fig. 1.

5 WW cross section results

The *CC03* cross sections in the various channels are obtained from the numbers of events selected in the data from

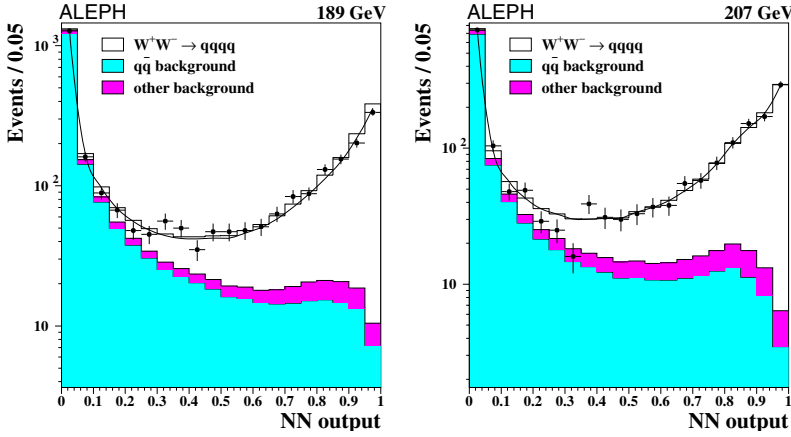


Fig. 3. Comparison of NN output distributions at 189 and 207 GeV for data and simulation in the fully hadronic channel after preselection. The dots correspond to the data and the histograms to the predictions. The solid curves show the results of the fits described in Sect. 5

Table 4. Fully leptonic cross sections. The quoted errors are statistical only. The typical systematic error in pb is indicated in the last row

Energy (GeV)	$\sigma(e\nu e\nu)$ (pb)	$\sigma(e\nu\mu\nu)$ (pb)	$\sigma(e\nu\tau\nu)$ (pb)	$\sigma(\mu\nu\mu\nu)$ (pb)	$\sigma(\tau\nu\mu\nu)$ (pb)	$\sigma(\tau\nu\tau\nu)$ (pb)	$\sigma(\ell\nu\ell\nu)$ (pb)
183	0.07 ± 0.05	0.37 ± 0.12	0.48 ± 0.12	0.17 ± 0.05	0.23 ± 0.10	0.11 ± 0.21	1.45 ± 0.20
189	0.16 ± 0.05	0.40 ± 0.07	0.42 ± 0.08	0.20 ± 0.04	0.35 ± 0.07	0.28 ± 0.08	1.78 ± 0.13
192	0.12 ± 0.10	0.44 ± 0.16	0.15 ± 0.16	0.28 ± 0.13	0.12 ± 0.13	0.36 ± 0.22	1.45 ± 0.29
196	0.21 ± 0.08	0.38 ± 0.10	0.37 ± 0.12	0.14 ± 0.06	0.45 ± 0.12	0.25 ± 0.12	1.78 ± 0.19
200	0.22 ± 0.08	0.43 ± 0.10	0.36 ± 0.12	0.25 ± 0.07	0.37 ± 0.11	0.20 ± 0.11	1.83 ± 0.19
202	0.26 ± 0.12	0.42 ± 0.14	0.27 ± 0.16	0.05 ± 0.07	0.52 ± 0.18	0.27 ± 0.18	1.78 ± 0.27
205	0.20 ± 0.09	0.33 ± 0.09	0.37 ± 0.13	0.11 ± 0.06	0.36 ± 0.11	0.14 ± 0.11	1.51 ± 0.18
207	0.15 ± 0.06	0.25 ± 0.07	0.45 ± 0.11	0.19 ± 0.06	0.56 ± 0.10	0.09 ± 0.09	1.69 ± 0.15
(syst.)	± 0.01	± 0.01	± 0.02	± 0.01	± 0.01	± 0.02	± 0.02

which the expected $4f - CC03$ difference and the various backgrounds are subtracted, corrected for the $CC03$ efficiencies. Systematic uncertainties are described in the next section.

WW $\rightarrow \ell\nu\ell\nu$

A maximum likelihood fit using Poissonian probability is applied to determine the cross section for each fully leptonic decay channel using efficiency matrices for $CC03$ processes and backgrounds. The total background amounts, on average, to 79 fb. The $(4f - CC03)$ correction amounts on average to $(+44 \pm 3)$ fb. It is dominated by $We\nu$ and ZZ events and the uncertainty comes from $4f$ events statistics.

The results of the fit for each channel and each CM energy are given in Table 4 together with the total fully leptonic cross sections extracted from the same fit assuming lepton universality.

WW $\rightarrow \ell\nu qq$

A similar fit to that used for the fully leptonic channels is performed, using the corresponding matrix of efficiencies and backgrounds. The partial cross sections are then extracted from a maximum likelihood fit to the number of events in each selection. The total background amounts,

on average, to 361 fb. The average $(4f - CC03)$ correction is $(+150 \pm 1.5)$ fb, dominated by $We\nu$ events.

Table 5 summarizes the cross section values for individual and inclusive semileptonic final states at each energy.

WW $\rightarrow qq qq$

The cross section is extracted by means of a binned maximum likelihood fit to the NN output distribution of data events where only the normalization of the WW $\rightarrow qq qq$ contribution is allowed to vary. All backgrounds are kept fixed both in shape and normalization. The fit results are given in Table 5.

Total W-pair cross section

The total cross section is obtained from a fit assuming the Standard Model branching fractions. The fit is applied at each CM energy to all data selected, as described in the previous sections, and uses the matrices of efficiencies and backgrounds for all the selections. The result would not be significantly different if the branching fractions of the Standard Model decay modes were unconstrained.

The results of the fits are given in Table 6. The table also summarizes the ratio R_{WW} of the measured cross section to the predictions of the most recent models YFSWW3

Table 5. Semileptonic and hadronic cross sections. The quoted errors are statistical only. The typical systematic error is indicated in the last row

Energy (GeV)	$\sigma(e\nu qq)$ (pb)	$\sigma(\mu\nu qq)$ (pb)	$\sigma(\tau\nu qq)$ (pb)	$\sigma(\ell\nu qq)$ (pb)	$\sigma(qqqq)$ (pb)
183	2.51 ± 0.25	2.15 ± 0.22	2.13 ± 0.29	6.82 ± 0.39	7.57 ± 0.42
189	2.36 ± 0.14	2.38 ± 0.13	2.41 ± 0.17	7.14 ± 0.23	6.88 ± 0.23
192	2.47 ± 0.36	2.48 ± 0.33	2.45 ± 0.43	7.40 ± 0.56	8.21 ± 0.61
196	2.47 ± 0.21	2.26 ± 0.19	2.65 ± 0.26	7.31 ± 0.34	7.51 ± 0.35
200	2.50 ± 0.21	2.56 ± 0.20	2.66 ± 0.26	7.70 ± 0.33	7.40 ± 0.33
202	2.91 ± 0.32	2.53 ± 0.28	2.47 ± 0.36	7.92 ± 0.49	6.96 ± 0.47
205	2.35 ± 0.21	2.47 ± 0.20	2.73 ± 0.27	7.47 ± 0.34	7.79 ± 0.35
207	2.46 ± 0.17	2.83 ± 0.17	2.68 ± 0.21	7.96 ± 0.27	7.73 ± 0.27
(syst.)	± 0.03	± 0.02	± 0.05	± 0.06	± 0.09

Table 6. Total WW cross sections at all CM energies and ratios to predictions from two calculations, **RacoonWW** and **YFSWW3**

Energy (GeV)	$\sigma(WW)(\text{pb})$ $\pm (\text{stat.}) \pm (\text{syst.})$	R_{WW} to RacoonWW $\pm (\text{stat.}) \pm (\text{syst.})$	R_{WW} to YFSWW3 $\pm (\text{stat.}) \pm (\text{syst.})$
183	$15.86 \pm 0.61 \pm 0.14$	$1.032 \pm 0.040 \pm 0.009$	$1.032 \pm 0.040 \pm 0.009$
189	$15.77 \pm 0.34 \pm 0.12$	$0.971 \pm 0.021 \pm 0.008$	$0.970 \pm 0.021 \pm 0.008$
192	$17.10 \pm 0.90 \pm 0.14$	$1.035 \pm 0.054 \pm 0.008$	$1.032 \pm 0.054 \pm 0.008$
196	$16.60 \pm 0.52 \pm 0.12$	$0.988 \pm 0.031 \pm 0.007$	$0.986 \pm 0.031 \pm 0.007$
200	$16.92 \pm 0.50 \pm 0.12$	$0.997 \pm 0.029 \pm 0.007$	$0.995 \pm 0.029 \pm 0.007$
202	$16.63 \pm 0.70 \pm 0.13$	$0.976 \pm 0.041 \pm 0.008$	$0.974 \pm 0.041 \pm 0.008$
205	$16.84 \pm 0.52 \pm 0.13$	$0.986 \pm 0.031 \pm 0.008$	$0.983 \pm 0.031 \pm 0.008$
207	$17.42 \pm 0.41 \pm 0.13$	$1.019 \pm 0.024 \pm 0.007$	$1.016 \pm 0.025 \pm 0.007$
combined		$0.995 \pm 0.011 \pm 0.007$	$0.993 \pm 0.011 \pm 0.007$

1.16 [20] and **RacoonWW** [25], which include the $\mathcal{O}(\alpha)$ electroweak radiative corrections. The expected uncertainty for **YFSWW3** and **RacoonWW**, evaluated as a function of the CM energy and of the W mass, varies from 0.5 to 0.7% [3]. Averaged over energies from 183 to 209 GeV, the measured cross section differs by $(-0.5 \pm 1.1 \pm 0.7)\%$ from **RacoonWW** predictions and by $(-0.7 \pm 1.1 \pm 0.7)\%$ from **YFSWW3**. Figure 4 shows the total cross section measured as a function of the CM energy compared with the **YFSWW3** and **RacoonWW** predictions. It includes the early measurements performed at WW threshold and 172 GeV energies [26].

6 Systematic uncertainties

The following subsections describe the different systematic uncertainties which affect the cross section measurement in each topology. A summary is given in Table 7. The uncertainties were evaluated at 189 GeV and 207 GeV and show no significant energy dependence.

Detector simulation

Systematic effects arise from inadequacies in the simulation of the detector response. Effects related to tracking

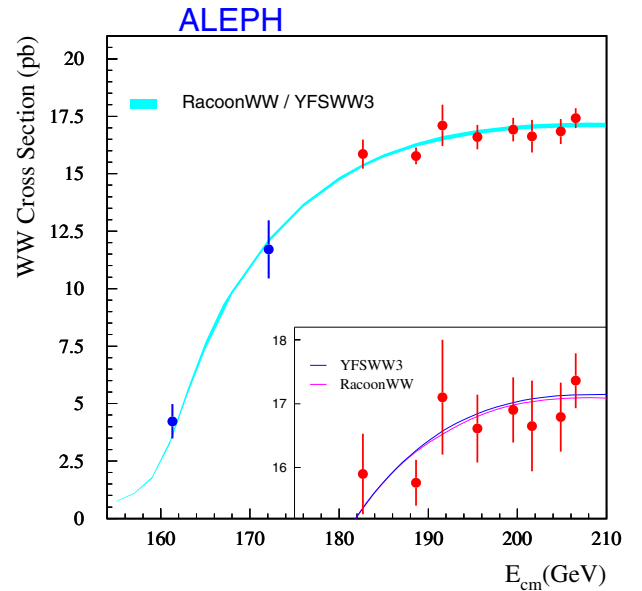
**Fig. 4.** Measurements of the W-pair production cross section at ten CM energies, compared to the Standard Model predictions from **YFSWW3** and **RacoonWW** for $m_W = 80.35 \text{ GeV}/c^2$

Table 7. WW cross section systematic uncertainty summary in fb evaluated at 207 GeV for each final state and for the total cross section. Correlations are taken into account where appropriate. The energy dependence has been evaluated and is propagated

Source	uncertainty (fb)			
	$\ell\nu\ell\nu$	$\ell\nu q\bar{q}$	$q\bar{q}q\bar{q}$	total
Tracking	4	19	31	54
Simulation of calorimeters	–	9	26	31
Hadronization models	–	27	8	35
Z peak $q\bar{q}$ fragmentation	–	–	20	20
Inter-W final state interaction	–	–	28	28
Background contamination	9	5	31	35
Lepton identification	1	2	–	3
Beam-related background	10	17	37	22
$\mathcal{O}(\alpha)$ corrections DPA	2	9	12	6
Luminosity	8	35	44	87
Simulation statistics	6	20	14	25
Total	17	57	87	126

and the calorimeter simulation and calibration have been studied. These affect mainly the four-quark and semileptonic selections.

- Tracking: the simulation of the tracking has been extensively studied using Bhabha and dimuon events from data at different energies. Corrections, derived from measured distortions, were applied to the data and the effect of these corrections on simulated events was used to estimate the systematic uncertainty. In addition random hit deletion was used to estimate the uncertainty arising from differing TPC efficiencies in data and simulation.
- Simulation of the calorimeters: a potential source of systematic error is related to the description of electromagnetic showers in the ECAL. To assess the related systematic effect, the noise levels and effects from incorrect photon energy corrections were examined. Possible inadequacies in the hadron calorimeter simulation have been assessed by applying a set of corrections to the simulated cluster energies, derived from data-simulation comparison.

Hadronization

Hadronization uncertainty effects have been studied by comparing various fragmentation models. The systematic error has been estimated by recomputing the cross section, using simulated signal events hadronized with HERWIG and ARIADNE. Both models have also been used to estimate hadronization uncertainties on the background for the semileptonic modes. The background for the fully hadronic final state is more complex as it comes from four-jet QCD production whilst the models are tuned to two-jet production at the Z. Although the tuning is appropriate for the $q\bar{q}q\bar{q}$ and $\ell\nu q\bar{q}$ signal due to the similarity of the Z and

W masses, it is not necessarily good for the four-jet QCD background in the $q\bar{q}q\bar{q}$ channel.

The same preselection used in the $WW \rightarrow q\bar{q}q\bar{q}$ analysis was applied to $Z \rightarrow q\bar{q}$ events after rescaling the jet energies, masses and multiplicities to take into account the centre-of-mass energy dependence. The NN output was calculated on these events and compared to the predictions of KK with different fragmentation models, JETSET and ARIADNE. The ratio of the data and simulation NN distributions at the Z resonance were used to correct the simulated background distributions at CM energies above the WW threshold. The measured WW cross section is shifted by 10 fb when the $q\bar{q}$ background is corrected for the difference between JETSET and data at the Z resonance. If ARIADNE is used instead, the observed shift is 20 fb. The latter value is taken as systematic uncertainty in the $q\bar{q}q\bar{q}$ channel.

Final state interactions

Possible final state interactions in the four-quark channel between particles from the decays of different W's have been investigated.

Bose-Einstein effects were simulated in the framework of PYTHIA for the model BE32 under the hypotheses of correlation between pions from the same W only and from either W. Colour reconnection effects were investigated in different implementations of the hadronization models (JETSET/SKI, HERWIG/11%, ARIADNE/AR2). The size of the observed shifts is approximately the same for all configurations.

Background contamination

The different background contributions in each channel are shown in Table 3. The background normalization has been varied by 2% for the $q\bar{q}$ and ZZ contributions, and 5% for the Zee contribution as suggested in [3]. For the $\gamma\gamma$ background a variation of 15% on the normalization is used, to take into account the data-simulation discrepancies. For this contribution, different models have been compared to evaluate possible additional discrepancies.

Lepton identification

The fully leptonic and the $(e, \mu)\nu q\bar{q}$ analyses use the efficiency correction factors given in Table 2. The statistical error on the correction factors, due to the limited size of the Z peak sample, is taken as an uncertainty. It amounts to 0.2% for electrons and 0.1% for muons. The lepton identification efficiency was also checked with dilepton events at high energies and showed no energy dependence within the statistical precision of the tests which is accounted as an extra uncertainty of 0.6% (0.4%) for electron (muon) identification, respectively. Events lost because of lepton identification inefficiency are in general selected in the tau channels. The associated systematic error on the total cross section is therefore kept at the level of 1–3 fb.

Beam-related background

Inefficiencies can occur due to non simulated beam-related background. In the $\ell\nu\ell\nu$ channel a cut is applied on the forward energy with a sizeable effect on the selection efficiency (Sect. 4.2). The uncertainty on this correction is propagated to the cross section measurement. In the other channels, the effect is much smaller and is taken as a systematic uncertainty.

Generator parameters

The simulation includes $\mathcal{O}(\alpha^3)$ leading log ISR radiative corrections. The third order corrections were conservatively taken as an uncertainty. The change in the cross section arising from different implementations of the DPA calculation in YFSWW3 is of the same order.

The effect of the W mass value uncertainty has also been evaluated. A change of 100 MeV/ c^2 changes the cross section by less than 5 fb.

Luminosity

The relative error on the integrated luminosity was kept each year below the 0.5% level. This uncertainty is correlated for all channels and each year. It is also partly correlated between years through the experimental error contribution and the theoretical precision.

Simulation statistics

In the hadronic channel, the uncertainty from finite Monte Carlo statistics has been evaluated by repeating the fit to the data, after fluctuating the content of each bin of the NN distribution according to Poisson statistics, for simulated signal and backgrounds. The RMS of the resulting Gaussian distribution is taken as the systematic error. For all other channels, straight error propagation is performed.

7 Branching fractions and V_{cs}

The W branching fractions are found by means of a fit to the data from all CM energies. The fit used to extract the total cross section is modified to allow the three individual leptonic branching fractions to vary, along with the eight total cross sections at 183, 189, 192, 196, 200, 202, 205 and 207 GeV. The hadronic branching fraction is set to $1 - B(W \rightarrow e\nu) - B(W \rightarrow \mu\nu) - B(W \rightarrow \tau\nu)$. The fitted leptonic branching fractions are

$$B(W \rightarrow e\nu) = 10.78 \pm 0.27 \text{ (stat.)} \pm 0.10 \text{ (syst.)}\%,$$

$$B(W \rightarrow \mu\nu) = 10.87 \pm 0.25 \text{ (stat.)} \pm 0.08 \text{ (syst.)}\%,$$

$$B(W \rightarrow \tau\nu) = 11.25 \pm 0.32 \text{ (stat.)} \pm 0.20 \text{ (syst.)}\%,$$

Table 8. W branching ratio systematic error breakdown in units of 10^{-4}

Source	uncertainty			
	$e\nu$	$\mu\nu$	$\tau\nu$	qq
Tracking	2.6	3.8	3.9	3.2
Simulation of calorimeters	1.6	2.4	2.0	5.9
Hadronization models	2.8	2.8	0.7	0.4
Z peak $q\bar{q}$ fragmentation	0.5	0.5	0.5	1.6
Inter-W final state interaction	1.9	1.9	1.9	5.7
Background contamination	1.9	2.4	2.6	6.4
Lepton identification	7.7	5.5	11.2	0.5
Beam-related background	2.5	1.4	15.4	10.2
$\mathcal{O}(\alpha)$ corrections DPA	0.4	1.1	3.1	1.7
Luminosity	0.8	0.5	0.3	1.5
Simulation statistics	1.0	0.7	1.4	1.4
Total	9.6	8.5	20.2	15.2

and are consistent with lepton universality and the Standard Model expectation. This result can be expressed also in terms of the lepton coupling ratios, as

$$g_\mu/g_e = 1.004 \pm 0.017 \pm 0.006,$$

$$g_\tau/g_e = 1.022 \pm 0.022 \pm 0.013,$$

$$g_\tau/g_\mu = 1.017 \pm 0.021 \pm 0.012.$$

The branching ratio systematic errors are computed by propagating the error from each channel to the global fit, taking into account correlations between channels and energies. The details are given in Table 8. The QCD part of the systematic error is defined as coming from the effect of different QCD generators for fragmentation as well as final state interactions. It amounts to 0.04% on the branching fraction in each channel. Due to cross-contaminations in the identification of W decays to $\tau\nu$ against $e\nu$ or $\mu\nu$, the measured $B(W \rightarrow \tau\nu)$ is 29% anticorrelated with $B(W \rightarrow e\nu)$ and 25% anticorrelated with $B(W \rightarrow \mu\nu)$. The $B(W \rightarrow e\nu)$ is 4.6% anticorrelated with $B(W \rightarrow \mu\nu)$.

If lepton universality is assumed, a fit of $B(W \rightarrow q\bar{q})$ and the eight total cross sections yields the hadronic branching fraction

$$B(W \rightarrow q\bar{q}) = 67.13 \pm 0.37 \text{ (stat.)} \pm 0.15 \text{ (syst.)}\%.$$

The QCD part of the systematic error is 0.10%. Using the world average value of $\alpha_s(m_Z^2) = 0.1187 \pm 0.0020$ [27] evolved to m_W^2 , $\alpha_s(m_W^2) = 0.121 \pm 0.002$, and assuming two quark families, this result can be expressed as a test of lepton-quark charged current universality:

$$\frac{g_q}{g_\ell} = 0.992 \pm 0.008 \pm 0.003.$$

The CKM matrix element V_{cs} can be evaluated as follows:

$$\frac{B(W \rightarrow q\bar{q})}{1 - B(W \rightarrow q\bar{q})}$$

$$= (|V_{ud}|^2 + |V_{cd}|^2 + |V_{us}|^2 + |V_{cs}|^2 + |V_{ub}|^2 + |V_{cb}|^2) \times (1 + \alpha_s(m_W^2)/\pi).$$

The sum of the squared CKM matrix elements [27] excluding V_{cs} is 1.048 ± 0.007 . The measured hadronic branching fraction is then interpreted as

$$|V_{cs}| = 0.958 \pm 0.017 (\text{stat.}) \pm 0.008 (\text{syst.}).$$

8 Conclusions

The W-pair production cross section has been measured at CM energies from 183 to 209 GeV in all W decay channels from an integrated luminosity of 683 pb^{-1} using a consistent set of simulated events and improved event selections.

The total cross sections are in agreement with the recent predictions of **RacoonWW** and **YFSWW3** (Fig. 4). The combined ratio R_{WW} of the measured total cross sections to the predictions is found to be $0.995 \pm 0.011 (\text{stat.}) \pm 0.008 (\text{syst.})$ for **RacoonWW** and $0.993 \pm 0.011 (\text{stat.}) \pm 0.008 (\text{syst.})$ for **YFSWW3**. The determination of individual branching fractions has been performed. The hadronic decay branching fraction is found to be $67.13 \pm 0.37 (\text{stat.}) \pm 0.15 (\text{syst.})\%$, which is used to determine the CKM matrix element $|V_{cs}| = 0.958 \pm 0.017 (\text{stat.}) \pm 0.008 (\text{syst.})$.

This result can be compared to similar ones published by other LEP experiments [28].

Acknowledgements. We would like to thank S. Dittmaier and W. Placzek for invaluable discussions. It is a pleasure to congratulate our colleagues from the CERN accelerator divisions for the successful operation of LEP throughout the LEP2 years. We are indebted to the engineers and technicians in all our institutions for their contributions to the excellent performance of ALEPH. Those of us from non-member countries thank CERN for its hospitality.

Appendix

A $\tau\nu q\bar{q}$ neural network input variables

The neural network $\tau\nu q\bar{q}$ event selection uses 15 variables, based on global event properties, tau and hadronic jet properties.

Global event properties:

- Total charged multiplicity.
- Visible mass(i.e. invariant mass of all energy-flow objects).
- Missing mass(i.e. mass associated to the missing momentum).
- Direction cosine of the missing momentum.
- Acollinearity of the two hemispheres of the hadronic part.
- Acoplanarity of the two hemispheres of the hadronic part.
- Missing energy.

- Energy in a wedge of half-angle 30° , with respect to the plane defined by the beam and the missing momentum direction.
- Energy in a cone of half-angle 20° around the direction of the missing momentum.

Tau and jet properties:

- Tau momentum.
- Isolation angle θ_j as defined in Sect. 4.3.2.
- The product (“tau quality” \times “isolation”), where “tau quality” =
 - 2 if the tau candidate satisfies all reconstruction criteria;
 - 1 if the tau fails the hadronic mass window but the hadronic mass is greater than $5 \text{ GeV}/c^2$;
 - 0 if the isolated jet candidate fails any other criteria.
 The “isolation” variable is defined in the text.
- Leading charged track energy in the tau jet.
- Energy of the least energetic hadronic jet.
- Energy of the most energetic hadronic jet.

B Hadronic neural network input variables

The neural network hadronic event selection uses 14 variables, based on global event properties, heavy quark flavour tagging, jet properties and WW kinematics. The four jets are numbered in order of decreasing energy.

Global event properties:

- Thrust.
- Sphericity.
- Missing energy.
- Sum of the four smallest interjet angles.

Heavy-flavour anti-tagging:

- Probability that all tracks come from the main vertex.

Jet properties:

- Maximum energy fraction of electromagnetic objects within a one-degree cone around any of the objects in any of the jets in the event.
- Maximum energy fraction of summed tracks in a jet.
- Smallest jet track-multiplicity.

WW kinematics:

- Angle between Jet 2 and Jet 3.
- The following jet related variables are determined from kinematically fitted jet momenta (Sect. 4.4).
- Energy of Jet 1.
- Energy of Jet 3.
- Energy of Jet 4.
- Smallest jet mass.
- Second smallest jet mass.

References

1. ALEPH Collab., Phys. Lett. B **453**, 107 (1999); Phys. Lett. B **484**, 205 (2000)
2. LEP2 Workshop, CERN 96-01, Vols. 1 and 2, eds. G. Altarelli, T. Sjöstrand and F. Zwirner (1996)
3. Reports of the working groups on precision calculations for LEP2 Physics, CERN 2000-009, eds. S. Jadach, G. Passarino and R. Pittau (2000)
4. ALEPH Collab., Nucl. Instrum. Methods A **294**, 121 (1990)
5. ALEPH Collab., Nucl. Instrum. Methods A **360**, 481 (1995)
6. ALEPH Collab., Z. Phys. C **53**, 375 (1992)
7. D.Bederede et al., Nucl. Instrum. Methods A **365**, 117 (1995)
8. S. Jadach et al., Comput. Phys. Commun. **102**, 229 (1997); B.F.L. Ward et al., UTHEP-98-0501 (1998)
9. S. Jadach et al., Comput. Phys. Commun. **140**, 475 (2001)
10. T. Sjöstrand, Comput. Phys. Commun. **82**, 74 (1994)
11. T. Sjöstrand et al., Comput. Phys. Commun. **135**, 238 (2001)
12. S. Jadach et al., Phys. Lett. B **390**, 298 (1997)
13. S. Jadach, B.F.L. Ward and Z. Wąs, Comput. Phys. Commun. **130**, 260 (2000)
14. J.A.M. Vermaseren, Proceedings of the IV International Workshop on Gamma Gamma Interactions, eds. G. Cochar, P. Kessler (1980)
15. G. Corcella et al., JHEP **0101**, 010 (2001)
16. L. Lönnblad, Comput. Phys. Commun. **71**, 15 (1992)
17. T. Sjöstrand, V.A. Khoze, Z. Phys. C **62**, 281 (1994); Phys. Rev. Lett. **72**, 28 (1994)
18. J. Rathsmann, Phys. Lett. B **452**, 364 (1999); A. Edin, G. Ingelman, J. Rathsmann, Phys. Lett. B **366**, 371 (1996); Z. Phys. C **75**, 57 (1997)
19. L. Lönnblad and T. Sjöstrand, Phys. Lett. B **351**, 293 (1995); Eur. Phys. J. C **2**, 165 (1998)
20. S. Jadach et al., Comput. Phys. Commun. **140**, 432 (2001)
21. W. Bartel et al., Z. Phys. C **33**, 23 (1986); S. Bethke et al., Phys. Lett. B **213**, 235 (1988)
22. Yu.L. Dokshitzer, J. Phys. G **17**, 1441 (1991)
23. D.Boumediene, Mesure de la masse du boson W^\pm dans l'expérience ALEPH, Thèse de Doctorat de l'Université Paris VI (2002), DAPNIA-2002-03-T and CERN-THESIS-2003-008
24. ALEPH Collab., Eur. Phys. J. C **17**, 241 (2000)
25. A. Denner, S. Dittmaier, M. Roth, D. Wackeroth, Nucl. Phys. B **560**, 33 (1999); Nucl. Phys. B **587**, 67 (2000); Phys. Lett. B **475**, 127 (2000); Eur. Phys. J. direct C **2**, 4 (2000)
26. ALEPH Collab., Phys. Lett. B **401**, 347 (1997); Phys. Lett. B **415**, 435 (1997)
27. The Particle Data Group, Phys. Rev. D **66**, 1 (2002)
28. DELPHI Collab., Eur. Phys. J. C **34**, 127 (2004); L3 Collab., Phys. Lett. B **496**, 19 (2000); OPAL Collab., Phys. Lett. B **493**, 249 (2000)